ORIGINAL PAPER

Simulation of single mode Rayleigh–Taylor instability by SPH method

M. S. Shadloo · A. Zainali · M. Yildiz

Abstract A smoothed particle hydrodynamics (SPH) solution to the Rayleigh–Taylor instability (RTI) problem in an incompressible viscous two-phase immiscible fluid with surface tension is presented. The present model is validated by solving Laplace's law, and square bubble deformation without surface tension whereby it is shown that the implemented SPH discretization does not produce any artificial surface tension. To further validate the numerical model for the RTI problem, results are quantitatively compared with analytical solutions in a linear regime. It is found that the SPH method slightly overestimates the border of instability. The long time evolution of simulations is presented for investigating changes in the topology of rising bubbles and falling spike in RTI, and the computed Froude numbers are compared with previous works. It is shown that the numerical algorithm used in this work is capable of capturing the interface evolution and growth rate in RTI accurately.

Keywords Smoothed particle hydrodynamics (SPH) · Mesh free method · Projection method · Multi-phase flow · Interfacial flow · Rayleigh–Taylor instability (RTI)

1 Introduction

Instability developing and evolving at the interface between two horizontal parallel fluids of different viscosities and densities with the heavier fluid at the top and the lighter one at the bottom is known as the Rayleigh–Taylor instability (RTI) to honor the pioneering works of Lord Rayleigh [1] and Taylor [2]. The instability initiates when a multiphase fluid system with different densities experiences gravitational force. As a result, an unstable disturbance tends to grow in the direction of gravitational field thereby releasing and reducing the potential energy of the system.

Due to being an important phenomenon in many fields of engineering and sciences, the RTI has been widely investigated by using experimental [3,4], analytical [5,6] as well as numerical [7,8] approaches. In the literature, one may find many qualitative mesh-dependent numerical studies for this two-phase flow problem [9–16]. There are also a few works that have used the smoothed particle hydrodynamics (SPH) method to model the RTI problem [17–21]. Cummins and Rudman [17] solved an RTI problem using the incompressible SPH (ISPH) approach which is based on the projection method. Tartakovsky and Meakin [18] modeled RTI problem in a multiphase and multi-component mixture with the weakly compressible SPH (WCSPH) method through solving momentum and species mass balance equations concurrently. Hu and Adams [19] used the combination of projection methods proposed and implemented by Cummins and Rudman [17] and Shao and Lo [20] and solved the RTI as a benchmark problem. More recently, Grenier et al. [21] presented a new WCSPH formulation for simulating interfacial flows, and modeled the RTI to validate their numerical scheme. All of these SPH works and some others simulated the RTI problem as a validation test case for the numerical algorithms. Surprisingly, out of the works which have been published up to now, there are only a few studies, especially for the long time evolution of the RTI, where the authors compare their numerical results with available analytical theories and if it is so, mesh dependent techniques were used [10,16], and to our best knowledge, there is no SPH work to

M. S. Shadloo · A. Zainali · M. Yildiz (✉)
Faculty of Engineering and Natural Sciences, Advanced Composites and Polymer Processing Laboratory, Sabanci University, Tuzla, 34956 Istanbul, Turkey
e-mail: meyildiz@sabanciuniv.edu

M. S. Shadloo
e-mail: mostafa@sabanciuniv.edu

date where the RTI problem is validated against analytical data.

SPH is a relatively new meshless numerical approach which has attracted significant attention in the last 15 years. Compared with the conventional mesh-dependent computational fluid dynamics (CFD) methods, the SPH approach exhibits unique advantages in modeling multiphase fluid flows and associated transport phenomena due to its capabilities of handling complex material surface behavior as well as modeling complicated physics in a relatively simple manner [22,23]. On the other hand, as SPH is still a developing CFD tool, it is vital to investigate its attributes, namely, advantages or potential limitations in modeling different multiphase flow problems to further understand and then improve this technique. Toward this end, this work aims to simulate the RTI problem by using the SPH method hence revealing its ability for capturing complex hydrodynamic instabilities and the physics in the RTI problem.

The paper is structured as follows: the presentation of the current work begins in Sect. 2 with a concise description of the numerical method. Afterward, governing equations and relevant boundary conditions for 2-D simulations are introduced in Sect. 3. The treatment of the interface for the multiphase flow and the solution algorithm are discussed in Sects. 4 and 5, respectively. Section 6 presents the results of simulations conducted for a droplet problem with the effect of surface tension force to validate the continuum surface force (CSF) model with analytical Laplace's solution, and a square-droplet deformation without the influence of surface tension to illustrate the nonexistence of artificial surface tension in the used SPH discretization scheme [18,24]. In the same section, the problem description for the RTI is provided along with simulation results validated by an analytical linear stability analysis. The long time evolution of the RTI is investigated and the comparison between the simulation results and existence theories are provided in details. The presentation is concluded in Sect. 7 with some final remarks.

2 SPH

Initially developed to solve astrophysics problems in 1977 by Gingold and Monaghan [25] and Lucy [26] in separate works, and later extended to solve a wide variety of fluid dynamics problems [27–29], SPH is a member of the family of Lagrangian methods. The SPH approach is based on smoothing the hydrodynamics properties of a fluid through a weighting/kernel function). The fluid in the solution domain is represented by the ensemble of movable points (also referred to as particles), which carry all relevant hydrodynamic properties such mass, density, and velocity, among others. The weighting function $W(r_{\mathbf{ij}}, h)$, or in short $W_{\mathbf{ij}}$, can be any arbitrary function (e.g., exponential, spline, and etc.) which

is required to posses some special properties [30] where $r_{\mathbf{ij}}$ is the magnitude of the distance vector ($\mathbf{r_{ij}} = \mathbf{r_i} - \mathbf{r_j}$) between a particle of interest $\mathbf{i}$ and its neighbor $\mathbf{j}$, $\mathbf{r_i}$ is a position vector defining the center point of the kernel function and h defines the length of the support domain of the particle of interest. The integral estimate or the kernel approximation to an arbitrary function $f(\mathbf{r_i})$, or $f_{\mathbf{i}}$ in a concise notation, evaluated at particle $\mathbf{i}$ can be introduced as

$$f_{\mathbf{i}} \cong \langle f_{\mathbf{i}} \rangle \equiv \int_{\Omega} f_{\mathbf{j}} W_{\mathbf{ij}} d^3 \mathbf{r_j}. \tag{1}$$

where $d^3\mathbf{r_j}$ is a differential volume element and Ω represents the total bounded volume of the domain.

Approximating the integration in Eq. (1) by the summation over particle $\mathbf{j}$ and setting $d^3\mathbf{r_j} = 1/\psi_{\mathbf{j}}$, one can write SPH interpolation for an arbitrary field $f_{\mathbf{i}}$ as

$$f_{\mathbf{i}} = \sum_{\mathbf{j}} \frac{1}{\psi_{\mathbf{j}}} f_{\mathbf{j}} W_{\mathbf{ij}}, \tag{2}$$

where the number density $\psi_{\mathbf{i}}$ for the particle $\mathbf{i}$ is defined as

$$\psi_{\mathbf{i}} = \sum_{\mathbf{j}} W_{\mathbf{ij}}, \tag{3}$$

which is approximately equal to reciprocal of the corresponding particle's volume $\psi_{\mathbf{i}} = \rho_{\mathbf{i}}/m_{\mathbf{i}}$.

The SPH approximation for the gradient of an arbitrary function $f_{\mathbf{i}}$ can be introduced as

$$\frac{\partial f_{\mathbf{i}}}{\partial x_{\mathbf{i}}^k} = \sum_{\mathbf{j}} \frac{1}{\psi_{\mathbf{j}}} f_{\mathbf{j}} \frac{\partial W_{\mathbf{ij}}}{\partial x_{\mathbf{i}}^k}, \tag{4}$$

For the sake of improving the accuracy and the stability of the SPH method, in the literature, several forms of corrective SPH gradient discretization formulations have been proposed and implemented with the aim of remedying particle inconsistency and kernel-boundary truncation related problems. Out of many excellent SPH studies that utilized the corrective SPH schemes, some deserves particular mention due to being the pioneering works in the field [31–37]. Randles and Libersky [31] used the renormalization procedure which modifies the gradient of the kernel function through utilizing two by two corrective matrix. Liu, Belytschko, and their co-workers [32–36] in series of papers used a reproducing kernel approach, which consists of a correction function and the conventional SPH kernel function and showed that their correction formulations removes the tensile instability [35]. It should be mentioned that many other corrective formulations are also possible. For example, Chen and Beraun in their work [37] also presented corrective SPH formulations for the first and the second order derivatives. Their first order derivative correction is quite similar to what has been utilized in this work. However, their second order derivative correction requires the inversion of three by three matrix unlike the

formulation presented in this work. In our earlier studies, we have attempted to use a corrective SPH formulation for the second-order derivative which also necessitates the inversion of three by three corrective matrix, and observed that three by three corrective matrix is rather sensitive to particle distribution, and becomes easily ill-conditioned, which is not the case for two by two corrective matrix [38].

Using a Taylor series expansion and the properties of a second-rank isotropic tensor, the corrective SPH approximation for the gradient of a vector-valued function can also be introduced as

$$\frac{\partial f_{\mathbf{i}}^p}{\partial x_{\mathbf{i}}^k} a_{\mathbf{i}}^{ks} = \sum_{\mathbf{j}} \frac{1}{\psi_{\mathbf{i}}} \left(f_{\mathbf{j}}^p - f_{\mathbf{i}}^p \right) \frac{\partial W_{\mathbf{ij}}}{\partial x_{\mathbf{i}}^s}, \tag{5}$$

where $a_{\mathbf{i}}^{ks} = \sum_{\mathbf{j}} \frac{1}{\psi_{\mathbf{j}}} r_{\mathbf{ji}}^k \frac{\partial W_{\mathbf{ij}}}{\partial x_{\mathbf{i}}^s}$ is a corrective second-rank tensor. The corrective term $a_{\mathbf{i}}^{ks}$ is ideally equal to Kronecker delta δ^{ks} for a continuous function. The corrective SPH discretization scheme for the Laplacian of an arbitrary function can be written in two different ways [38,22]

$$\frac{\partial}{\partial x_{\mathbf{i}}^k} \left(\zeta_{\mathbf{i}} \frac{\partial f_{\mathbf{i}}^p}{\partial x_{\mathbf{i}}^k} \right) = 8 \left(a_{\mathbf{i}}^{pm} \right)^{-1} \sum_{\mathbf{j}} \frac{2}{\psi_{\mathbf{j}}} \frac{\zeta_{\mathbf{i}} \zeta_{\mathbf{j}}}{\zeta_{\mathbf{i}} + \zeta_{\mathbf{j}}} f_{\mathbf{ij}}^p \frac{r_{\mathbf{ij}}^p}{r_{\mathbf{ij}}^2} \frac{\partial W_{\mathbf{ij}}}{\partial x_{\mathbf{i}}^m}, \tag{6}$$

$$\frac{\partial}{\partial x_{\mathbf{i}}^k} \left(\zeta_{\mathbf{i}} \frac{\partial f_{\mathbf{i}}^p}{\partial x_{\mathbf{i}}^k} \right) = \frac{8}{(1 + a_{\mathbf{i}}^{ll})} \sum_{\mathbf{j}} \frac{2}{\psi_{\mathbf{j}}} \frac{\zeta_{\mathbf{i}} \zeta_{\mathbf{j}}}{\zeta_{\mathbf{i}} + \zeta_{\mathbf{j}}} f_{\mathbf{ij}}^p \frac{r_{\mathbf{ij}}^s}{r_{\mathbf{ij}}^2} \frac{\partial W_{\mathbf{ij}}}{\partial x_{\mathbf{i}}^s}, \tag{7}$$

where ζ might denote μ, and ρ^{-1}, and $f_{\mathbf{ij}}^p = f_{\mathbf{i}}^p - f_{\mathbf{j}}^p$. In a multiphase system with a large mismatch in transport parameters such as density and viscosity of phases, the attentive treatment of interface fluxes or gradients is of significant importance for the accuracy and the robustness of the computation. Therefore, it is a common practice in the SPH approach to smooth transport parameters through using a weighted harmonic mean interpolation, namely $\zeta_{\mathbf{i}} = 2\zeta_{\mathbf{i}}\zeta_{\mathbf{j}}/(\zeta_{\mathbf{i}} + \zeta_{\mathbf{j}})$, as has been done in above equations.

It is to be mentioned that in our early works [38,22], Eqs. (5) through (7) were written based on the particle density (not in terms of the number density $\psi_{\mathbf{i}}$) and were used to treat single phase problems. In this work, Eq. (6) is used for the discretization of the Laplacian of velocity field in the linear momentum equation while Eq. (7) is utilized for the Laplacian of pressure in the pressure Poissons equation. Finally in the present simulations, the compactly supported 2-D quintic spline is used

$$W_{\mathbf{ij}} = \chi \begin{cases} (3-q)^5 - 6(2-q)^5 + 15(1-q)^5 & 0 \le q \le 1 \\ (3-q)^5 - 6(2-q)^5 & 1 \le q \le 2 \\ (3-q)^5 & 2 \le q \le 3 \\ 0 & 3 \le q \end{cases} \tag{8}$$

Here, $q = r_{\mathbf{ij}}/h$ and the spline coefficient χ is equal to $\frac{7}{478}\pi h^2$ for 2-D quintic spline.

3 Governing equations

We consider Newtonian, viscous, incompressible, and immiscible two-phase system. The governing equations for such a system are the conservation of mass and linear momentum, which are respectively formulated in Lagrangian form as

$$\frac{D\rho}{Dt} = -\rho \nabla \cdot \mathbf{v}, \tag{9}$$

$$\rho \frac{D\mathbf{v}}{Dt} = \nabla \cdot \underline{\mathbf{t}} + \mathbf{f}^{vs} + \rho \mathbf{f}^b, \tag{10}$$

where $\mathbf{v}$ is the fluid velocity vector, ρ is the fluid density, $\underline{\mathbf{t}}$ is the total stress tensor, $\mathbf{f}^b$ is the body force which is equal to gravitational force in this work, and $\mathbf{f}^{vs}$ is the volumetric surface tension force. The total stress tensor is defined as $\underline{\mathbf{t}} = -p\underline{\mathbf{I}} + \underline{\mathbf{T}}$, where p is the absolute pressure, $\underline{\mathbf{I}}$ is the identity tensor, and $\underline{\mathbf{T}} = \mu(\nabla \mathbf{v} + (\nabla \mathbf{v})^T)$ is the viscous part of the total stress tensor, where μ is the dynamic viscosity. Finally, D/Dt is the material time derivative operator.

4 Computation of the surface tension force

The surface tension force acts on the interface between two fluids. The balance of linear momentum at the interface can be formulated as $\mathbf{f}^s = \sigma \kappa \mathbf{n}$ for the constant surface tension coefficient. Here $\mathbf{f}^s$ is the surface tension force per unit area which acts on the interface in the unit normal direction, σ is the surface tension coefficient, $\mathbf{n}$ is the unit normal vector to the interface, and κ is the curvature of the interface. For the sake of computational simplicity and efficiency, it is preferable to express this local surface force as an equivalent volumetric force $\mathbf{f}^{vs}$ (the force per unit volume) as is done in the CSF method originally proposed by Brackbill et al. [10]. The basic concept behind this approach is to replace the sharp interface between two fluids with a transition region of a finite thickness. This can be realized through multiplying the surface tension force per unit area with the delta Dirac function δ^s as

$$\mathbf{f}^{vs} = \sigma \kappa \delta^s \mathbf{n}. \tag{11}$$

The volumetric surface tension force $\mathbf{f}^{vs}$ acts only on the interface along the unit normal direction, and vanishes in the bulk of the fluid. The effect of the surface tension is consequently included in the computational model in the form of an external force term.

To be able to distinguish among constituents of an immiscible multiphase system, and calculate relevant interface fields (i.e., the interface unit normal, curvature, and

interfacial forces), each particle is assigned to color function such that $c = 0$ for fluid 1 and $c = 1$ for fluid 2. To avoid sharp variations in the color function across the interface, the color function for each particle is smoothed as

$$C_i = \frac{\sum_j W_{ij} c_j}{\sum_j W_{ij}}. \tag{12}$$

Here, it should be noted that the smoothed color function C_i effectively represents the volume fraction of fluid 2, namely, $C_i^{(2)} = C_i$ and $C_i^{(1)} = 1 - C_i$ wherewith one can write $\sum_\alpha C_i^\alpha = 1$ where C_i^α is the smoothed color function of α th phase.

Each fluid particle has constant ρ and μ. Since ρ and μ are discontinuous across the interface, the numerical scheme might have instabilities especially in the case of a large mismatch in the transport parameters of constituents. Hence, it is practical to smooth the density and the viscosity of fluids through using a weighted arithmetic mean interpolation. Upon using smoothed color function, the density and viscosity of the multiphase system can be calculated from those of constituents respectively as

$$\rho_i = (1 - C_i)\rho_1 + C_i\rho_2, \tag{13}$$

and

$$\mu_i = (1 - C_i)\mu_1 + C_i\mu_2. \tag{14}$$

The unit normal vector $\mathbf{n}$ for particle $\mathbf{i}$ can be calculated as

$$\mathbf{n} = \nabla C / |\nabla C|. \tag{15}$$

Unit normals in the vicinity of fringes of the interface might be erroneous and in turn may produce faulty results when they are used in the computation of the curvature. Therefore, a constraint is required to determine reliable normals as also pointed out in [39]. In this direction, the constraint in the form of $|\nabla C_i| > \epsilon/h$ is employed. Here, ϵ is a constant used to control the thickness of the interface, which is set to be $\epsilon = 0.08$ in this work. Particles satisfying this condition are regarded to be interface particles with reliable unit normals.

Further, upon using only these reliable normals, the curvature for particle $\mathbf{i}$ is calculated as

$$\kappa = -\nabla \cdot \mathbf{n}. \tag{16}$$

Finally, substituting Eqs. (15) and (16) into Eq. (11), and approximating the delta Dirac function as the magnitude of the gradient of the color function $|\nabla C|$, one can rewrite the volumetric surface force as,

$$\mathbf{f}^{vs} = -\sigma(\nabla \cdot (\nabla C / |\nabla C|))\nabla C. \tag{17}$$

5 Numerical scheme

In this section, we describe the sequence of the numerical procedure implemented in this work. The modeling domains of each test case are represented by particles generated on a Cartesian grid with equidistant particle spacing. Physical boundaries of the computational domain are defined by a row of fixed particles whose relevant fields are evolved in accordance with the numerical solution. Boundary and fluid particles are distinguished through associating them with different integer label. Moreover, boundary particles with dissimilar boundary conditions are also differently labeled so that one can implement various boundary conditions when necessary. The transport parameters and initial conditions are assigned to both fluid and boundary particles. All fluid and boundary particles are given the same smoothing lengths as $h = \eta r_{ij,o}$ where $r_{ij,o}$ is the initial particle spacing, and η is a problem-dependent input parameter. In the present work, a constant smoothing length with $\eta = 1.6$ is used.

The neighbor list is formed for each particle utilizing a standard box-search algorithm, and then ghost particles are generated for the utilization of multiple boundary tangents (MBT) boundary treatment in the numerical procedure. The details of the MBT method can be found in our earlier works [40,38]. The field values Γ (i.e., velocities, and pressure) of a ghost particle are obtained depending on the type of boundary condition implemented. For the Dirichlet boundary condition which specifies values for field variables on the boundary of the domain, the following linear interpolation is utilized; namely, $\Gamma_g = 2\Gamma_b - \Gamma_f$ where Γ_g, Γ_b, and Γ_f are the fields variables of the ghost, boundary, and fluid particles, respectively. As for the Neumann boundary condition which specifies values for the field variables as a derivative on the boundary, a ghost particle is assigned to the same field values as the corresponding fluid particle, namely, $\Gamma_g = \Gamma_f$. Besides, ghost particles are bestowed with the same mass, density, number density, and viscosity as their corresponding fluid particles.

The mass of particles is calculated using the relation $m_i = \rho_i/\psi_o$ where $\psi_o = max(\psi_i)$ is the initial or reference number density. In what follows, one can notice that particles of dissimilar phases are to have different masses which are kept constant throughout the simulation. Having entered into the outermost time loop of the numerical algorithm, the time step is calculated adaptively through satisfying the so-called Courant–Friedrichs–Lewy (CFL) condition as $\Delta t \leq ch/V_{max}$ with $c = 0.25$ in this work.

Then, at each time step, before moving fluid particles to their temporary or intermediate position, the average particle spacings $r_{i,o}$ for all fluid particles are computed as $r_{i,o} = \sum_j r_{ij}/N$ (with N being the number of neighbors for particle $\mathbf{i}$), which is followed by the calculation of the artificial particle displacement (APD) vector $\delta\mathbf{r_i} = \beta V_{max} r_{i,o}^2 \sum_j \mathbf{r_i}/r_{ij}^3$ for

all fluid particles where β is a problem-dependent parameter which is set to be equal to 0.02 for all test cases [38,22].

With the knowledge of divergence free velocity $\mathbf{v_i}^{(n)}$, and particle position $\mathbf{r_i}^{(n)}$ at time n, all fluid particles are advected to their temporary or intermediate positions

$$\mathbf{r_i}^* = \mathbf{r_i}^{(n)} + \mathbf{v_i}^{(n)} \Delta t + \delta \mathbf{r_i}. \tag{18}$$

where relatively small APD vector is added to the above given advection equation with the aim of disturbing the particle trajectories hence preventing local particle clusterings or fractures in the computational domain which are inherent to SPH method and known to be one of the sources of tensile instability problem.

Due to the fact that particles have been moved to their intermediate positions, their neighbors (both real and ghost particles) need to be updated. Depending on the magnitude of the velocity fields, one may assume that the neighbors of a given particle may not change significantly. Thus, to reduce the computational burden incurred due to the neighbor finding and ghost particle-creation algorithms, the neighbor lists and ghost particles are updated every tenth time step. Afterward, in the interface subroutine, the surface tension force is computed, and the mass and the viscosity of the mixture are calculated through using a weighted arithmetic mean interpolation as $m_\mathbf{i} = \sum_\alpha m_\mathbf{i}^\alpha C_\mathbf{i}^\alpha$ and $\mu_\mathbf{i} = \sum_\alpha \mu_\mathbf{i}^\alpha C_\mathbf{i}^\alpha$.

One of the most efficient ways to solve the balance of linear momentum equation is the projection method by which the momentum balance equation is decoupled from the continuity equation. The projection method relies on the principle of Hodge decomposition whereby any vector field can be decomposed into a divergence-free part and the gradient of an appropriate scalar potential such that

$$\mathbf{v_i}^* = \mathbf{v_i} + \frac{\Delta t}{\rho} \nabla p_\mathbf{i}^{(n+1)}. \tag{19}$$

Upon taking the divergence of Eq. (19), one can obtain the pressure Poisson equation as

$$\frac{\nabla \cdot \mathbf{v}^*}{\Delta t} = \nabla \cdot \left(\frac{\nabla p}{\rho} \right), \tag{20}$$

noting that the term $\nabla \cdot \mathbf{v}$ is set to be zero due to the assumption of incompressibility. In the pressure Poisson equation, the divergence of the intermediate velocity acts as a source term. Eq. (20) is subjected to the Neumann boundary condition

$$\left(\frac{\rho}{\Delta t} \right) (\mathbf{v}^* - \mathbf{v}) \cdot \mathbf{n} = \nabla p \cdot \mathbf{n}, \tag{21}$$

that can be obtained by projecting Eq. (19) on the outward unit normal vector $\mathbf{n}$ to the boundary. The pressure boundary condition can be further simplified to a form of $\nabla p \cdot \mathbf{n} = 0$ with the assumption that the boundary conditions for the divergence free velocity are used for the intermediate velocity, namely, $(\mathbf{v}^* - \mathbf{v}) \cdot \mathbf{n} = 0$.

The intermediate velocity field $\mathbf{v}^*$ is calculated on the intermediate particle locations by solving the momentum balance equations with forward time integration without the pressure gradient term as

$$\mathbf{v_i}^* = \mathbf{v_i}^{(n)} + \mathbf{f_i}^{(n)} \Delta t, \tag{22}$$

together with pertinent boundary conditions, where $\mathbf{f_i}$ represents the right hand side of the linear momentum equation.

Given the intermediate particle positions and velocities, the intermediate number densities and divergences of intermediate velocities are calculated, which are used in the pressure Poisson equation. The intermediate number density is calculated through the solution of the mass conservation in the following form

$$\psi_\mathbf{i}^* = \psi_\mathbf{i}^{(n)} - \Delta t \psi_\mathbf{i}^{(n)} \left(\nabla \cdot \mathbf{v_i}^* \right). \tag{23}$$

The pressure Poisson equation is solved together with the Neumann boundary condition using a direct solver based on the Gauss elimination method to calculate the pressure $p_\mathbf{i}^{(n+1)}$ wherewith the incompressibility condition can be enforced. The intermediate number and mixture densities are used when solving the pressure Poisson equation where intermediate mixture density is calculated as

$$\rho_\mathbf{i}^* = \psi_\mathbf{i}^* \sum_\alpha m_\mathbf{i}^\alpha C_\mathbf{i}^\alpha. \tag{24}$$

Then the divergence-free velocities are obtained by

$$\mathbf{v_i}^{(n+1)} = \mathbf{v_i}^* - \underbrace{\frac{\Delta t}{\rho} \nabla p_\mathbf{i}^{(n+1)}}_{I}. \tag{25}$$

To be able to treat large variation in the density across the interfaces in a robust manner without facing pressure related convergence issues, the discretization of the pressure gradient term I in Eq. (19) requires a special treatment. Upon using the product rule of differentiation, one can write that

$$\frac{1}{\rho} \nabla p = \nabla \left(\frac{p}{\rho} \right) - p \nabla \left(\frac{1}{\rho} \right), \tag{26}$$

whose right hand side can be discretized by using Eq. (5) as

$$\frac{1}{\rho} \nabla p_\mathbf{i}$$
$$= \left(a_\mathbf{i}^{ks} \right)^{-1} \left(\sum_\mathbf{j} \frac{1}{\psi_\mathbf{j}} \left[\left(\frac{p_\mathbf{j}}{\rho_\mathbf{j}} - \frac{p_\mathbf{i}}{\rho_\mathbf{i}} \right) - \left(\frac{p_\mathbf{i}}{\rho_\mathbf{j}} - \frac{p_\mathbf{i}}{\rho_\mathbf{i}} \right) \right] \frac{\partial W_\mathbf{ij}}{\partial x_\mathbf{i}^s} \right)$$
$$= \left(a_\mathbf{i}^{ks} \right)^{-1} \left(\sum_\mathbf{j} \frac{1}{\rho_\mathbf{j} \psi_\mathbf{j}} (p_\mathbf{j} - p_\mathbf{i}) \frac{\partial W_\mathbf{ij}}{\partial x_\mathbf{i}^s} \right). \tag{27}$$

It is noted that in the calculation of the pressure gradient in Eq. (27), the intermediate number density and mixture densities are used. Finally, with the correct velocity field for
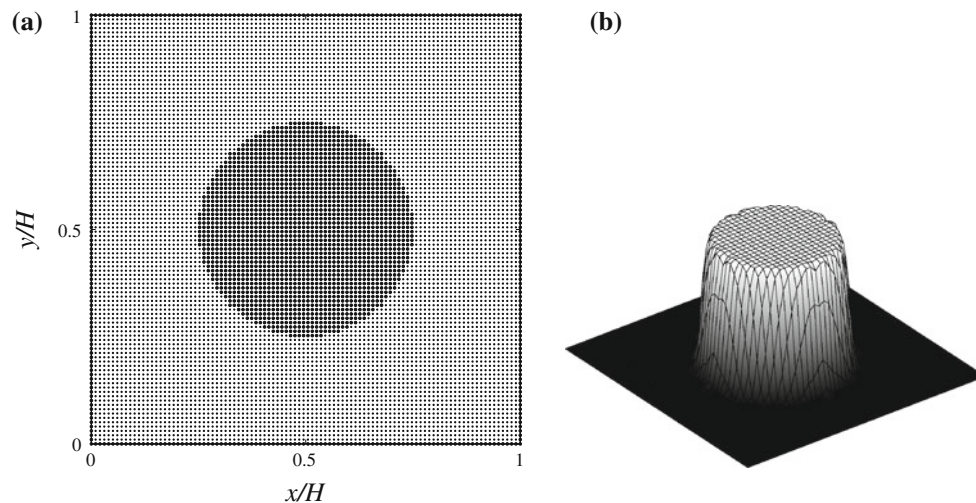
Fig. 1 **a** Initial particle distribution for the circular droplet (fluid 2) surrounded by the background fluid (fluid 1) and **b** pressure field for the over all domain. The particle resolution is 100×100

time-step $n + 1$, all fluid particles are moved to their new positions

$$\mathbf{r_i}^{(n+1)} = \mathbf{r_i}^{(n)} + 0.5 \left(\mathbf{v_i}^{(n)} + \mathbf{v_i}^{(n+1)} \right) \Delta t + \delta \mathbf{r_i}. \qquad (28)$$

At the end, neighbor and ghost particles lists are updated, and then the initial (reference) number density of the fluid is restored. For further details of the numerical algorithm, readers are referred to our earlier work [38].

6 Results

In the following, we consider three test cases, two of which are modeled to validate the accuracy of the surface tension force and the numerical scheme used while the last one is performed to reveal the ability of the SPH method for capturing the physics behind the hydrodynamic instabilities in the RTI problem correctly.

6.1 Laplace's law

A static circular bubble is a commonly used test case for validating the accuracy of numerically computed pressure jump across the interface in multiphase systems since it has a simple analytical solution, $(p_{in} - p_{out} = \sigma/r)$, widely referred to as Laplace's law for a stationary droplet [16,41]. The computational domain for this test case is a unit square with H denoting the edge length and a circular bubble with a radius of $r = 0.25$ m is placed at the center of the unit square domain ($H = 1$ m, see Fig. 1a). It is represented by an array of 100 by 100 particles in x- and y-directions, and the smoothing length for all particles is set equal to 1.6 times the initial particle spacing.

The simulation parameters are density, viscosity and surface tension coefficient with the numerical values of $\rho_1 = \rho_2 = 1000$ kg/m^3, $\mu_1 = \mu_2 = 1$ Pa s and $\sigma = 0.25$ N/m, respectively. The utilized model parameters, namely, the radius of the bubble and the surface tension, should lead to pressure jump of unity on the interface in accordance with the Laplace relation $p_{in} - p_{out} = \sigma/r = 1$ Pa. As for the boundary conditions, the pressure on the boundaries is set equal to zero, and the no-slip boundary condition is imposed for velocity on all solid walls. The initial velocity field is zero.

As stated previously, in the numerical modeling of multiphase flows, the physically sharp interface is approximated by a transition region of a finite thickness, and the surface tension force is included in the momentum balance equation as a volumetric force that is active only over this finite interface thickness through the usage of Dirac delta function. Thus, it is numerically impossible to reproduce sharp or exact pressure jump as in the case of analytical solution [16] since the pressure jump across the interface is smoothed. The existence of this smoothed pressure gradient, and also the slight variation of curvature along the perimeter of the circular bubble due to the discrete nature of the numerical approach induce spurious or parasite currents which are observed as vortices in the vicinity of interface despite the absence of any external force. Not only are they inherent to the CSF method but also observed in other surface tension methods which use the discrete delta function approach [12,42]. Figure 1b presents the computed pressure field for the over all domain.

Figure 2 illustrates the locations of the spurious currents in the neighborhood of the interface for two different mesh resolutions for the first time step. It is seen from the figure
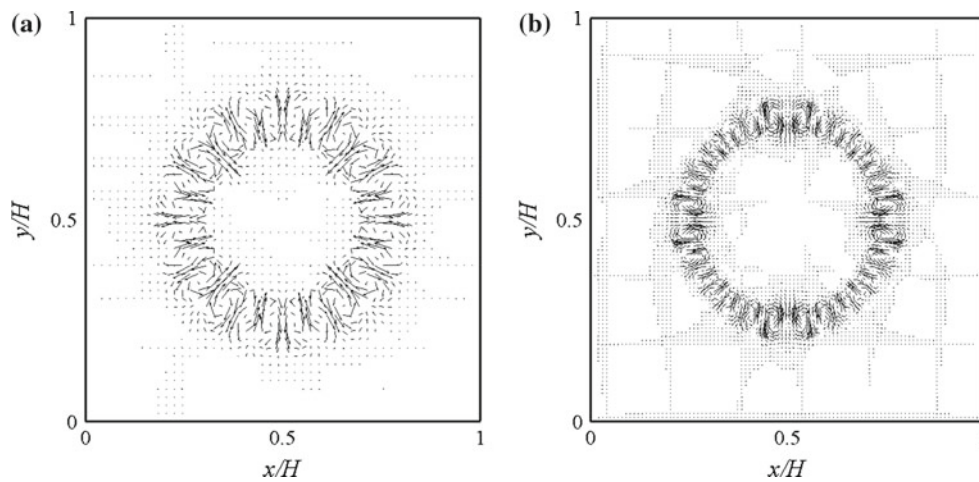
Fig. 2 The locations of the spurious currents in the neighborhood of the interface for the particle resolutions of **a** 50×50 and **b** 100×100

Table 1 The L_1 and L_2 norms of velocity magnitude after the first time step

Particle resolution	L_1 norm	L_2 norm
25×25	8.64e−6	1.64e−6
50×50	4.64e−6	6.4e−7
100×100	3.64e−6	2.4e−7
200×200	2.64e−6	1.35e−7

that the spurious current can be alleviated through the mesh refinement. In spite of the spurious current, it is observed that the computed pressure gradient across the interface is equal to $p_{\text{in}} - p_{\text{out}} = 1.004$ Pa which is in a good agreement with the analytical result. Here, the pressure inside and outside the bubble is calculated by averaging the pressure fields of particles for fluids 2 and 1 which are far enough from the interface. Since the parasitic current in this test case in the energy point of view is at least two order of magnitude lower than the applied surface tension force, it does not create any serious effect on the results; nevertheless, in some problems, force due to the spurious effect might be comparable to other physical forces such as viscous, gravitational, and surface tension forces, among others, thereby leading to over/underestimated erroneous values in computational results.

To show the convergence of the numerical model, in Table 1 are given the L_1 and L_2 norms of the velocity magnitude for the same time step, which are respectively defined as $L_1 = \sum_i^N \|\mathbf{v}\|/N$ and $L_2 = \sqrt{\sum_i^N \|\mathbf{v}\|^2/N^2}$. Given that the simulation starts with zero initial velocity field, the interface velocities after the first time step are a direct measure for the error in the pressure fields. As seen from Table 1, as the particle resolution increases, both L_1 and L_2 norms decrease, which indicates the convergence due to the particle refinement.

6.2 Square droplet

The presence of velocity field on the interface of two fluids in the absence of any external forces due to the jump in the density of phases across the interface is known as artificial surface tension [24]. This is an undesired non-physical phenomenon which is directly related to the discretization scheme and the treatment of density discontinuity. The artificial surface tension can introduce some error into the model thereby leading to inaccurate calculation of curvature, and the formation of unphysical flow across the interface. Square droplet problem is one of the simplest test cases which can be used effectively to demonstrate if the artificial surface tension exists in the solution domain. For this benchmark problem, the domain geometry and the boundary conditions are identical to the first one except that the bubble is replaced by a square droplet. The density ratio of phases is $R = \frac{\rho_2}{\rho_1} = 5$ where $\rho_1 = 1000$ kg/m^3 and the kinematic viscosity is kept constant, which is equal to $\nu_1 = \nu_2 = 10^{-3}$ m^2/s.

Figure 3 shows particle positions for $t = 0$, and $t = 1$ s. Unlike the standard SPH [18], both sub figures are identical to each other, which indicates that the particle number density formulations used in the discretization of governing equations do not generate any artificial surface tension.

6.3 RTI

The RTI can occur in a multiphase fluid system where a layer of heavier fluid is placed on top of another layer of lighter fluid with an interface having a small initial perturbation. This disturbance grows, and subsequently produce a spike of heavier fluid moving downward into the lighter fluid and bubbles of the lighter fluid moving upward. For modeling the RTI phenomena, a rectangular computational domain (Fig. 4) with the width and the height of H and $4H$
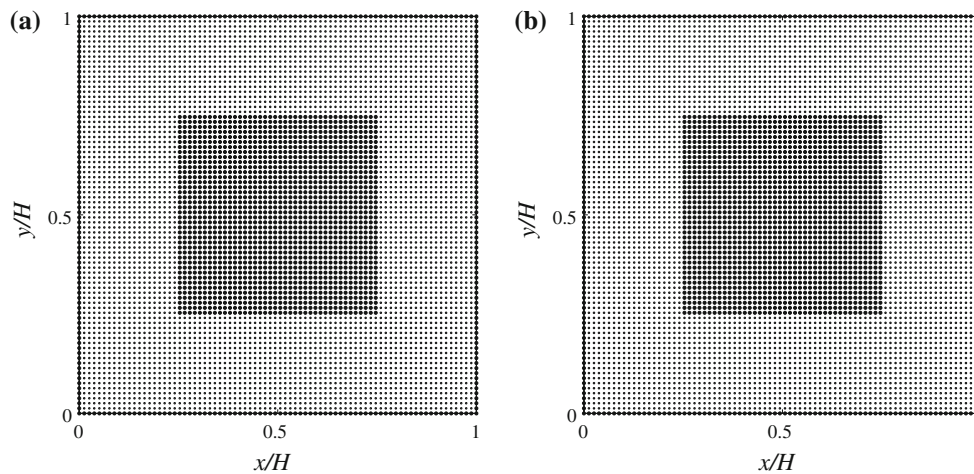
Fig. 3 **a** Initial particle distribution of a square drop of fluid 2 surrounded by fluid 1 and **b** the particle distribution for the same problem after 1 s

is used. For simplicity, H is chosen to be unity (H=1 m). The number of particles for each fluid region is the same. Fluid and boundary particles are given the same smoothing lengths as $h = 1.6r_{\mathbf{ij},o}$. An initial sinusoidal perturbation, $y = 2 + \xi_o \cos(kx)$, is applied to the fluid–fluid interface through swapping the color fields of particles in the vicinity of the perturbation where ξ_o is the amplitude of the applied disturbance, which is $\xi_o = 0.05H$, k is the wave number $k = 2/\pi\lambda$, and λ is the wave length which is set to be $\lambda = 1$ m.

In all simulations, the density of the heavier fluid layer is set to be $\rho_1 = 1000$ kg/m³ and kinematic viscosity for both fluids are kept constant, which is equal to $\nu_1 = \nu_2 = 10^{-3}$ m²/s. The body force taken as gravity (g) acts only in downward direction on all particles with the numerical value of 0.09 m/s². The boundaries are treated as solid walls, and the no-slip and zero pressure gradient boundary conditions are imposed using the MBT method [40].

In accordance with the linear theory for RTI [43], the initial sinusoidal perturbation of the interface grows exponentially in time, and the growth rate is given by

$$\gamma^2 = kg\left[A_T - \frac{k^2\sigma}{g(\rho_1 + \rho_2)}\right], \quad (29)$$

where $A_T = \frac{\rho_2 - \rho_1}{\rho_2 + \rho_1} = \frac{R-1}{R+1}$ is the Atwood number. It should be noted that Eq. (29) is the well-known exact analytical solution for inviscid fluids subjected to surface tension. Considering the effect of viscous force, Mikaelian [6] presented an accurate analytical approximation for the asymptotic growth rate of viscous flow in the linear regime in the form of

$$\gamma^2 - \frac{\mu_1 + \mu_2}{\rho_2}(1 + A_T)k^2\gamma - \left[A_T kg - \sigma k^3 \frac{1 + A_T}{2\rho_2}\right] = 0, \quad (30)$$

which deviates from the exact solution less than 11 %.

Upon setting $\gamma^2 = 0$ in Eq. (29), one can calculate the maximum or critical surface tension, $\sigma_c = (\rho_2 - \rho_1)g/k^2$, below which the given perturbation is unstable, namely, $\sigma < \sigma_c$ where σ_c is the critical surface tension and shows the border of instability. In what follows, one can introduce an stability parameter as

$$\phi = \sigma/\sigma_c, \quad (31)$$

where $\phi > 1$ means that the two-fluid system should be stable.

Figure 5 compares analytical and numerical growth rates in the linear regime which are plotted as a function of stability parameter where γ_e, $(\gamma_{x1}, \gamma_{x2})$, and γ_n denote respectively the growth rate for inviscid flow, the roots of growth rate for viscous flow, and the numerical growth rate, which are correspondingly calculated from Eqs. (29) and (30) and

$$\gamma_n = \frac{\hat{\xi}/\xi_o - 1}{t}. \quad (32)$$

Here t is the simulation time at which the perturbation amplitude $\hat{\xi}$ is approximately equal to $\hat{\xi} \approx 0.1H$. It should be noted that there is a good agreement between analytical and numerical results except for some higher values of the stability parameter. However, all results follow the same pattern.

Figure 6 presents the results of numerical simulations with the density ratio of $R = 2$ which corresponds to $A_T = 1/3$ for various stability parameters, namely, $\phi = 0.0, 0.2, 0.6, 0.9,$ and 1.1. In all cases, results are plotted for dimensionless time $t^* = t(g/H)^{0.5} = 9.0$. Simulation results show an exponential growth for $\phi < 1.15$ and a stable oscillation for $\phi > 1.15$.

The close observation of Fig. 6 suggests that the morphology of the instability for the unstable regime can be
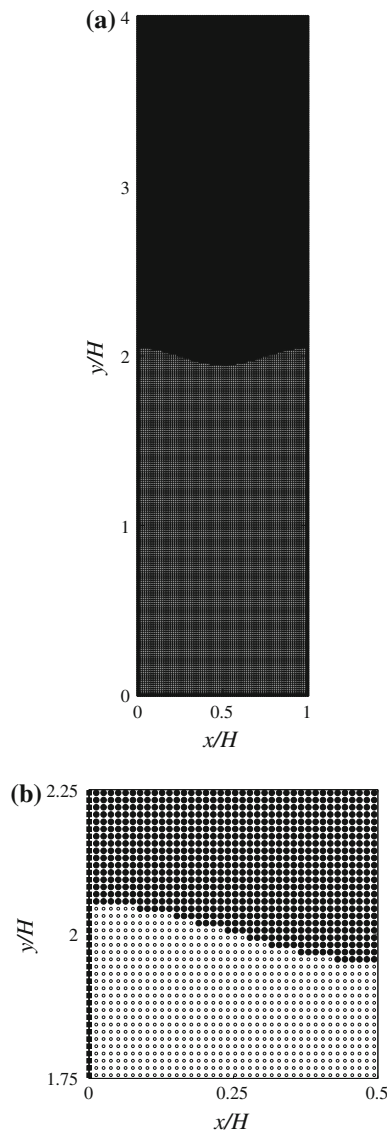
(a)

(b)

Fig. 4 **a** Initial uniform particle distribution for RTI and **b** the zoomed in view of the initial uniform particle distribution for the left half of the domain. The particle resolution is 80×320
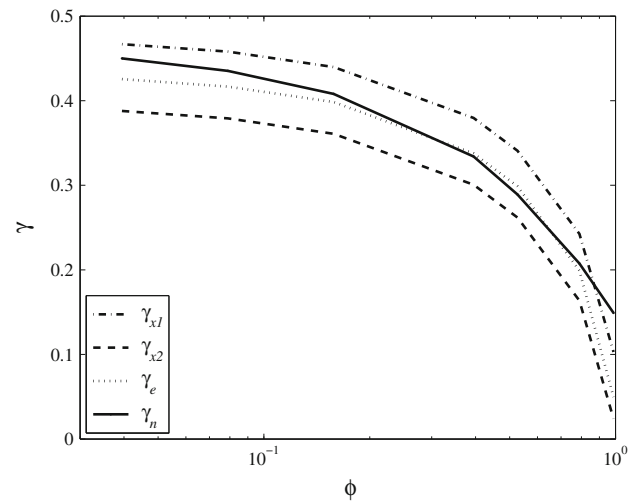

Fig. 5 The dependence of the linear growth rate γ of a disturbance on its stability parameter ϕ for the Atwood number of $A_T = 1/3$

hindered (see Fig. 6d, e). It is noted that although according to Eq. (31), the border of instability is marked by the stability parameter of unity $\phi = 1.0$, here we have found that this value is equal to $\phi \approx 1.15$ which deviates by 15 % from the analytical calculation. Several reasons might contribute to this discrepancy.

The first reason might be initial particle distribution. Recalling that the computational domain is initially represented by a Cartesian grid with a equidistant particle spacing, and then the sinusoidal perturbation is formed through swapping the color fields of particles in the vicinity of the planar interface, it is rather difficult to obtain highly smooth and continuous initial sinusoidal disturbance due to the discreteness in the particle distribution, as seen in Fig. 4b. This may result in several smaller wave-like structures on the main wave length. In the course of simulations, especially for initial times in the linear regime, these wave-like structures may act as additional disturbances which tend to grow, hence causing over prediction of the growth rate and the stability parameter. Another reason might be spurious currents due to the usage of CSF model for the surface tension. As elaborated in Sect. 6.1, the spurious current brings about unphysical velocity field in the vicinity of the interface, which causes extra kinetic energy therein, thereby shifting the RTI problem toward instable region. Finally, the numerical diffusion owing to the smoothing nature of the SPH method for variables such as density, viscosity, pressure, among others, especially in the neighborhood of the interface might also contribute to the deviation in the stability parameter since it consumes the stabilizing surface energy due to the surface tension.

Time evolution of the fluid interface of the single mode perturbation RTI for the stability parameter of $\phi = 0.0$ and $\phi = 0.4$ are shown in Figs. 7 and 8, respectively. Here, results
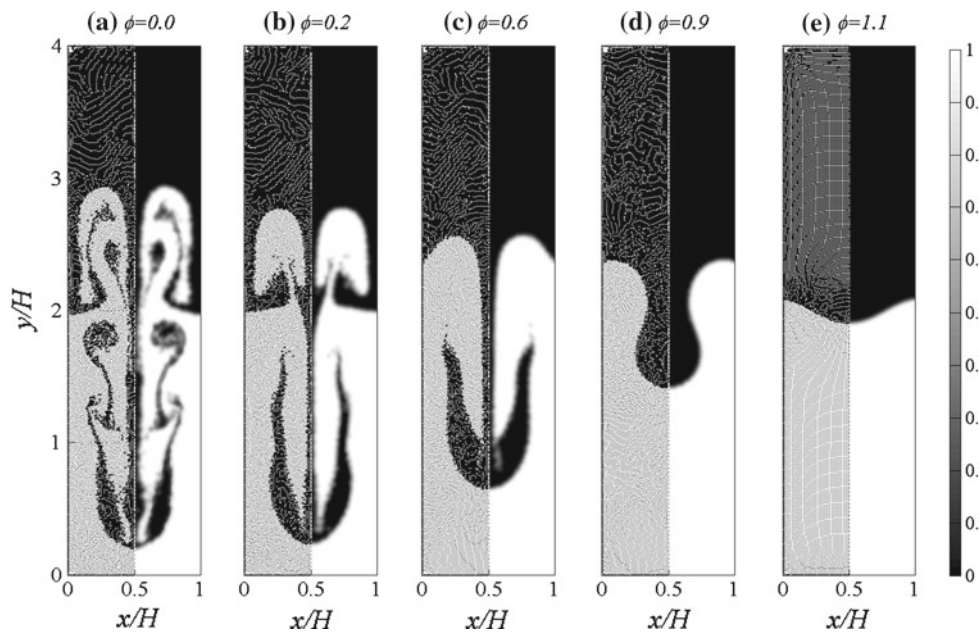
divided into three visible categories. The first category is associated with small stability parameter values due to rather small surface tension. In this category, the gravitational force dominates over the surface tension force, hence causing the spike to accelerate into the lighter fluid. As a result, one can notice the formation of secondary vortices, so called Kelvin–Helmholtz instability, on the bubble-spike interface owing to the interfacial shear (see Fig. 6a, b). The second category is observed when the gravitational and interfacial forces are comparable. In this case, although the spike has its side tails, the shear due to the acceleration is not so strong to lead to the creation of secondary instabilities (see Fig. 6c). In the last category corresponding to higher values of stability parameter, where the surface tension force is dominant, the instability is

Fig. 6 The evolution of the fluid interface of the single mode perturbation RTI for the Atwood number of $A_T = 1/3$ at dimensionless time of $t^* = t(g/H)^{0.5} = 9$. The *left hand side* of each sub figures presents particle distributions whereas the *right hand side* indicates the contour plots of the color function for the stability parameter values of **a** $\phi = 0.0$, **b** $\phi = 0.2$, **c** $\phi = 0.6$, **d** $\phi = 0.9$, and **e** $\phi = 1.1$
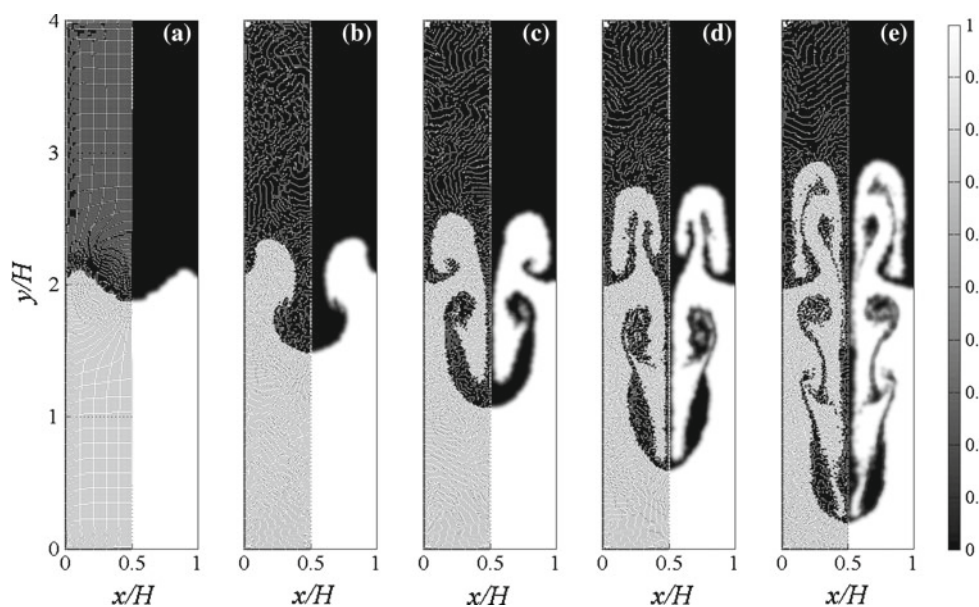

Fig. 7 Time evolution of the fluid interface of the single mode perturbation RTI for the Atwood number of $A_T = 1/3$ and the stability parameter of $\phi = 0.0$. The *left panels* of each sub figures show particle distributions while the *right panels* illustrate contour plots of the color function for dimensionless times of **a** $t^* = 1.8$, **b** $t^* = 3.6$, **c** $t^* = 5.4$, **d** $t^* = 7.2$, and **e** $t^* = 9.0$

are presented for five equidistant dimensionless times with $0 \leq t^* = t(g/H)^{0.5} \leq 9.0$.

Upon disturbing the initial planar interface sinusoidally, the hydrostatic pressure acts to drive the heavier fluid into the lighter one with the disturbance amplitude initially growing exponentially. Shortly afterward, a "mushroom cap" shape

begins forming. As the time progresses, the heavy fluid falling down gradually forms a central spike with two side tails which shed side spikes from their ends for the lower stability parameter case. Eventually, for the first case where $\phi = 0.0$, the main spike of the heavy fluid experiences the Kelvin–Helmholtz instability while two side spikes are stretched and
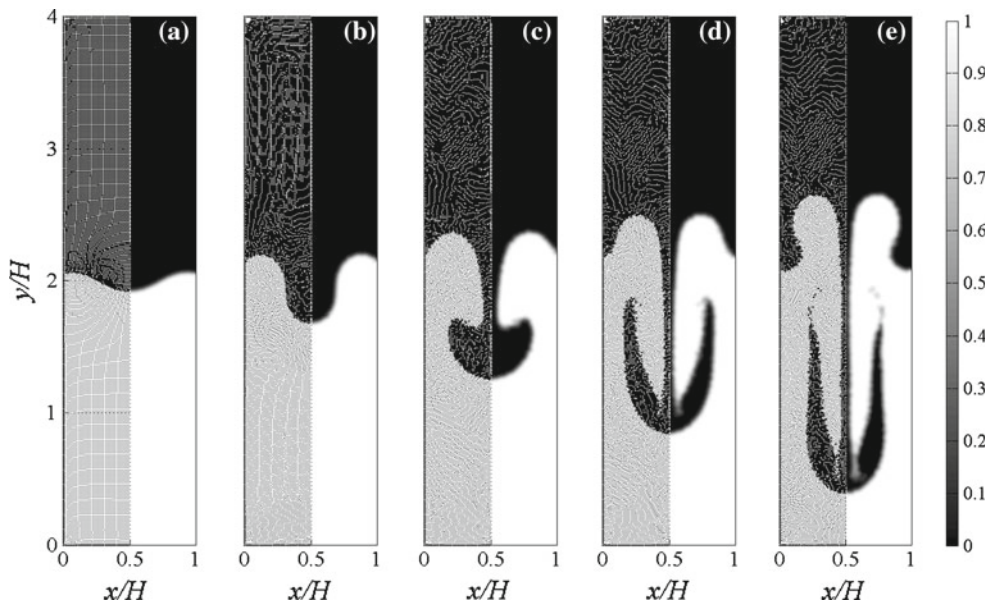
Fig. 8 Time evolution of the fluid interface of the single mode perturbation RTI for the Atwood number of $A_T = 1/3$ and the stability parameter of $\phi = 0.4$. On the *left panels* are given particle distributions while on the *right panels* are presented contours of the color function for dimensionless times of **a** $t^* = 1.8$, **b** $t^* = 3.6$, **c** $t^* = 5.4$, **d** $t^* = 7.2$, and **e** $t^* = 9.0$

folded into very complicated shapes. On the other hand for the second case ($\phi = 0.4$), the interface along the central spike, as well as the fronts of both bubble and the spike remain relatively smooth.

The features of RTI during the time evolution can be better illustrated via the velocity fields. For this reason, the velocity vectors and magnitudes for the same set of data are presented in Figs. 9 and 10. As expected, the heavier fluid falls down in the middle and the lighter fluid rises along vertical walls. A distorted single vortex is clearly visible at the initial time for both cases. For the lower stability parameter case (see Fig. 9), a strong shear layer exists, which provides a good condition for the formation of secondary instabilities. In this situation, with an increase in time, more and more vortices are generated and the flow field becomes quite distorted along both side of the domain. However, an increase in the stability parameter (or an increase in the surface tension) significantly suppresses the development of both Kelvin–Helmholtz instability and the tails roll-up and the interface along the instability remains rather smooth (see Fig. 10). In this case, up to late time, the dilute single vortex still exists and elongates along the domain height. The interfacial patterns obtained in this work compare very well with those in [13,44].

In Figs. 11 and 12, the positions and velocities of the bubble's fronts and spike's tips, h_b, v_b and h_s, and v_s respectively, are plotted as a function of time for the test case presented in Fig. 6. As expected, the lower the stability parameter, the higher the bubble front (Fig. 11a) and the faster the bubble velocity (Fig. 11b). The bubble velocity is one of the impor-

tant characteristic behaviors of RTI which attracted the attention of researchers [45–47]. The single bubble is found to rise with the steady velocity of [48]

$$v_b = Fr \sqrt{\frac{\rho_2 - \rho_1}{\rho_2} \frac{g D_b}{2}}, \tag{33}$$

where Fr is the Froude number (a dimensionless number which is defined as the ratio of inertial to gravitational forces and is used to quantify resistance of an object moving through a fluid), and D_b is the bubble diameter. If D_b is taken to be approximately equal to λ and with some simple mathematical manipulation, the following relationship for Fr can be obtained:

$$Fr = \frac{v_b}{\sqrt{\frac{A_T}{1 + A_T} g \lambda}}. \tag{34}$$

It is noted that Eqs. (33) and (34) does not take into account the dilution of bubbles due to the entrainment of heavier fluid and any physical and numerical diffusions.

Calculating the magnitude of bubble velocity from numerical results, one can obtain the Fr number for the bubble motion as presented in Fig. 13. Evidentially, it is shown that two well known analytical solutions proposed by Goncharov [46] and Abarzi et al. [47] form the lower and the upper bounds for the simulation results. Additionally, the presented velocity and Fr number patterns are consistent with those reported in literature [49,50].
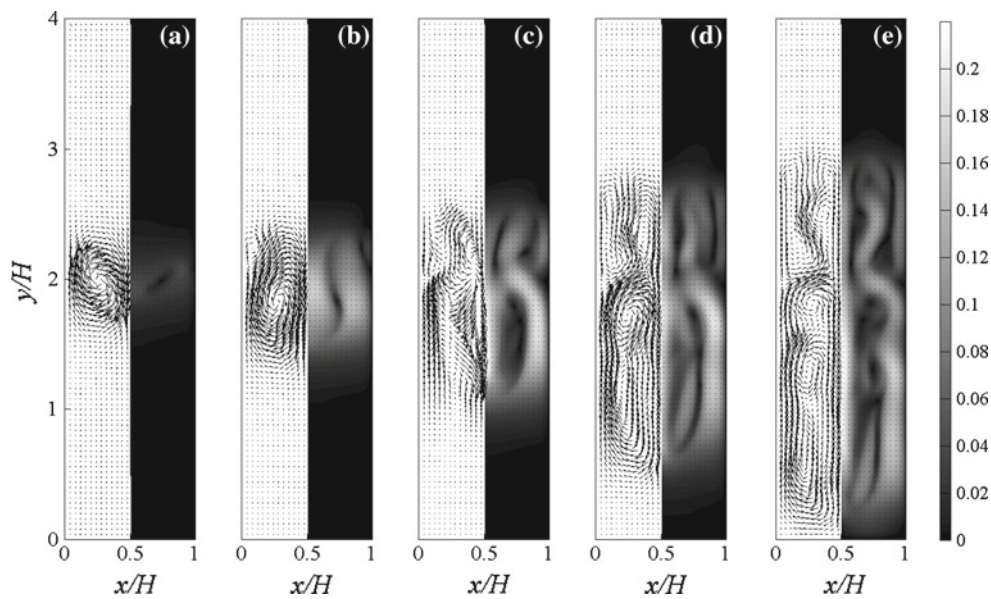
Fig. 9 Time evolution of velocity fields of the RTI for the Atwood number of $A_T = 1/3$ and the stability parameter of $\phi = 0.0$. The *left hand sides* of sub figures denote velocity vectors while the *right hand sides* show velocity contours (m/s) (the interval between contours is 0.02) for the dimensionless time of **a** $t^* = 1.8$, **b** $t^* = 3.6$, **c** $t^* = 5.4$, **d** $t^* = 7.2$, and **e** $t^* = 9.0$
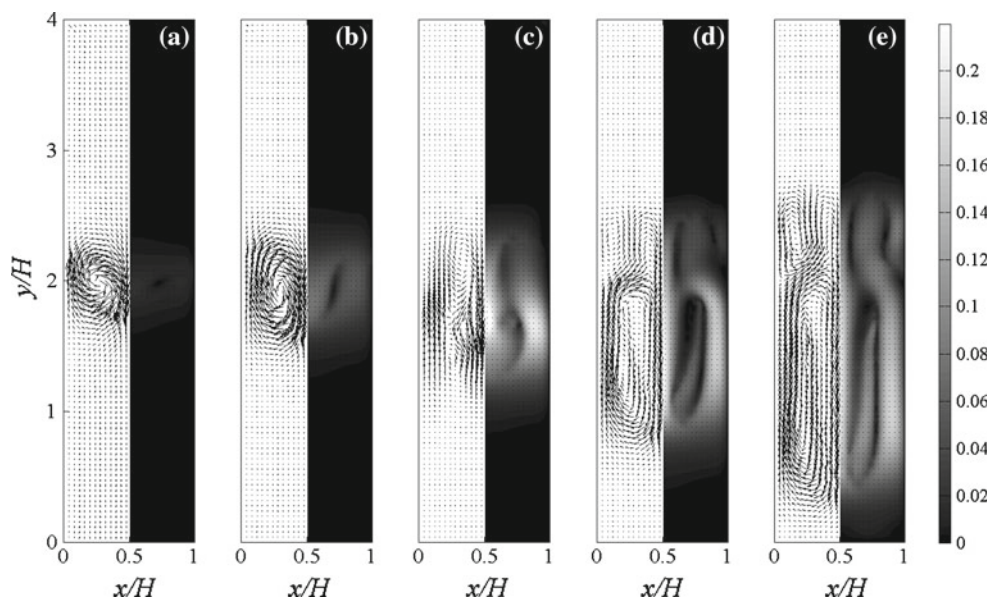

Fig. 10 Time evolution of velocity fields of the RTI for the Atwood number of $A_T = 1/3$ and the stability parameter of $\phi = 0.4$. The *left hand sides* of sub figures denote velocity vectors while the *right hand sides* show velocity contours (m/s) (the interval between contours is 0.02) for the dimensionless time of **a** $t^* = 1.8$, **b** $t^* = 3.6$, **c** $t^* = 5.4$, **d** $t^* = 7.2$, and **e** $t^* = 9.0$

The sensitivity of the numerical solutions to particle numbers has also been investigated through solving a test case with the Atwood number of $A_T = 1/3$ and the stability parameter of $\phi = 0.4$ on three different sets of particles (i.e., 60×240 (coarse), 80×320 (intermediate), and 120×480 (fine)). Results of these simulations are summarized as; the interface position at dimensionless time of $t^* = 4.5$ in

Fig. 14a, and the y-coordinates of the tip of the falling (spike) and rising (bubble) fluid as function of dimensionless time in Fig. 14b. Figure 14a demonstrates evidently that the intermediate particle number provides solutions with sufficient accuracy considering the trade-off between computational costs and capturing the features being studied. Additionally, Fig. 14b indicates that the bubble position is well reproduced
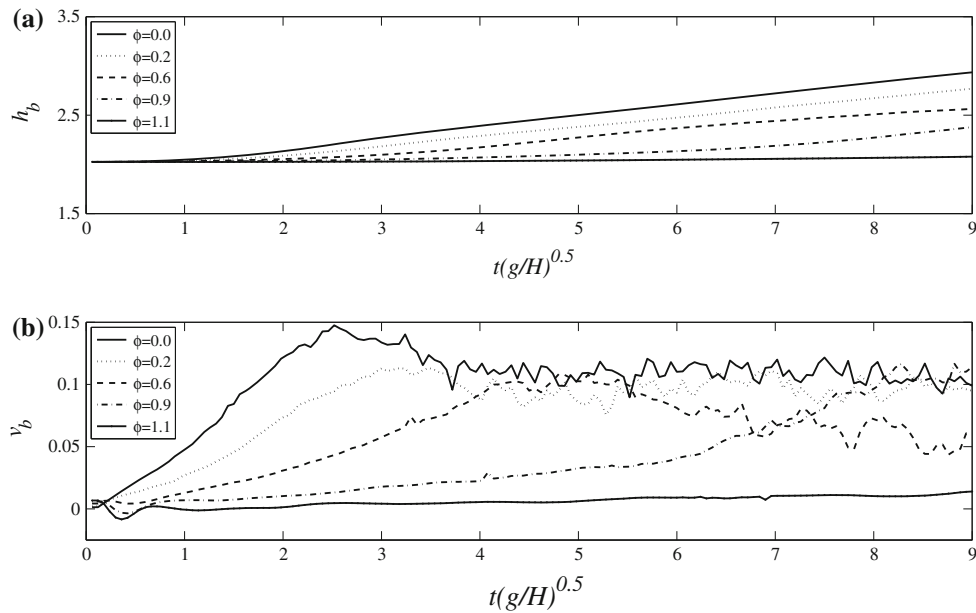
Fig. 11 a The y-coordinate positions and **b** the velocities of the tip of the rising fluid (bubble) versus dimensionless time at the Atwood number of $A_T = 1/3$ for various stability parameters, namely, $\phi = 0.0, 0.2, 0.6, 0.9,$ and 1.1
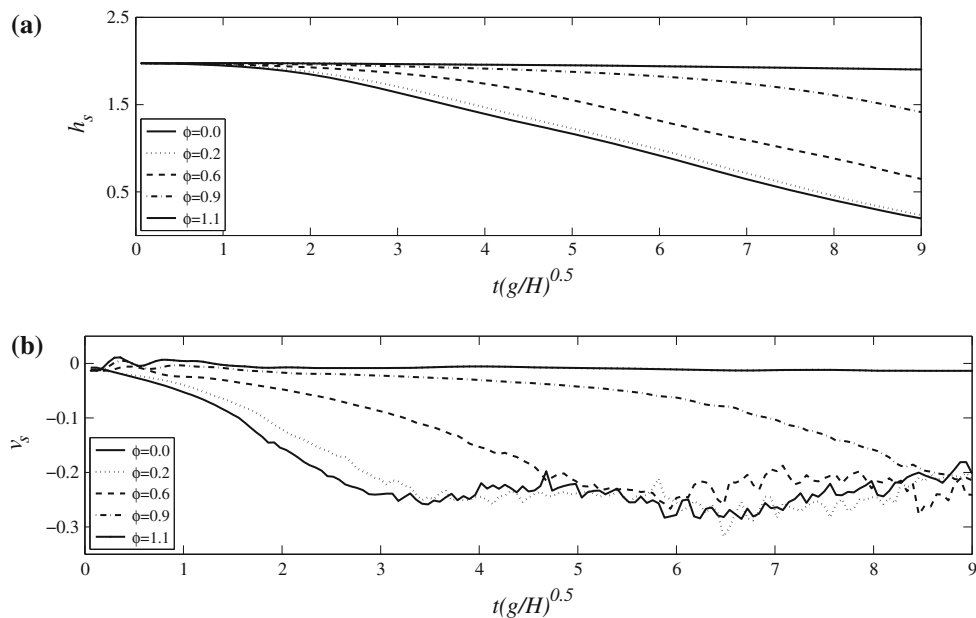

Fig. 12 a The y-coordinate positions and **b** the velocities of the tip of the falling fluid (spike) versus dimensionless time at the Atwood number of $A_T = 1/3$ for various stability parameters, namely, $\phi = 0.0, 0.2, 0.6, 0.9,$ and 1.1

by using coarse particle number, but the spike appears to need at least the intermediate particle resolution in order to achieve convergence. Therefore, in this work, all RTI results are obtained using intermediate particle resolution.

Like many other works on the numerical simulation of RTI in literature, the previously presented results have been obtained utilizing initially uniform Cartesian particle distribution (referred to as cubic grid hereafter). For the sake of completeness, to be able assess possible difficulties caused

by irregular distributions of particles, numerical experiments with initially non-uniform particles have also been conducted; namely, staggered Cartesian grid and two different forms of circular grid (radially centered, and radially off-centered) with nearly equal particle spacing as illustrated in Fig. 15b, c, and d, respectively. Particles for circular grids are generated following the procedure described. Initially, particle spacing is determined in accordance with the dimensions of domain boundaries and the number of particles in the
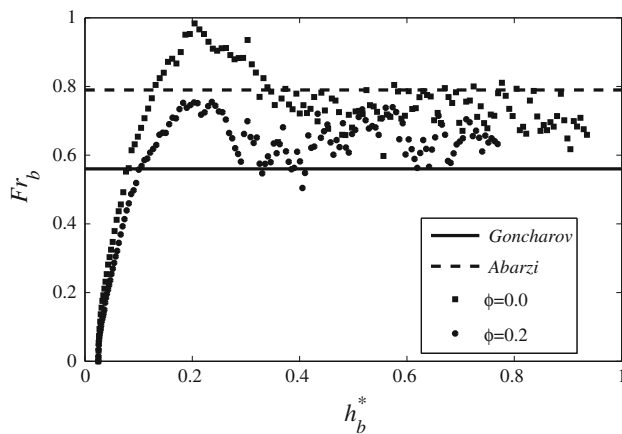
Fig. 13 The Froude number of the rising fluid (bubble) versus dimensionless bubble tip position at the Atwood number of $A_T = 1/3$. The *solid* and the *dashed lines* are the analytical solutions proposed by Goncharov [46] and Abarzi [47] respectively, and the it square and *circle* points represent the simulation results for the values corresponding to stability parameters $\phi = 0.0$, and $\phi = 0.2$ respectively. The dimensionless bubble tip position is calculated as $h_b^* = h_b/\lambda$

x- and y-direction of the Cartesian grid. Then, the largest boundary length is chosen as a radius for the greatest circle. This radius is divided into particles with the same particle spacing as the boundary particles. Accordingly, the position of each particle on the radius of the largest circle (i.e., $4H$ for the current computational domain configuration) is used as the radius for other smaller circles. The number of particles to be generated on each circle is determined in a way that the particle spacing is equal. Once particles are generated in circular manner on all circles, the rectangular computational domain is extracted from the domain represented by particles with circular arrangement. Simulation parameters for numerical experiments conducted on these irregular particle distributions are identical to one presented in Fig. 7c. The number of particles for cubic grid, staggered grid, radially centered

and off-centered grids is 25600, 25600, 25974, and 25989, respectively. It is noted that the non-uniform particle distribution makes it impossible to construct a symmetric disturbance with respect to vertical central line. Due to the discreteness of the particles, the initial amplitudes of the disturbances for circular grids are slightly different from cubic and staggered grids, and circular grids have larger y-coordinate positions for the tip of the spike than cubic and staggered grids with respect to bottom horizontal wall of the domain. As can be seen from Fig. 15f–h, these issues lead to the development of asymmetry in the spike of the instability, and inconsistencies among simulation results in terms the position of the tip of the spike as well as the straightness of the stem of the spike since the initial cosine shape disturbance is no longer a perfect cosine function and also there are also several wavelike disturbances on the main wave which change the form of the initial disturbance. To conclude, even though as the simulation progress, all fluid particles acquire random distribution, it appears that the initial particle distribution is quite important to be able construct a symmetric and a smoothly varying disturbance.

7 Conclusion

The SPH method has been used for the simulation of incompressible multiphase flow where the interfacial dynamics are modeled by the CSF model. Numerical simulations were carried out for three different 2-D problems namely, circular and square droplet, and RTI developed from the single-mode initial perturbation. Our simulations for the first two problems validate the accuracy of the implemented CSF model and also show the non-existence of artificial surface tension in the used numerical scheme while the last problem reveals most features of RTI observed in previous theoretical and numerical studies. For the single-mode RTI, both initial
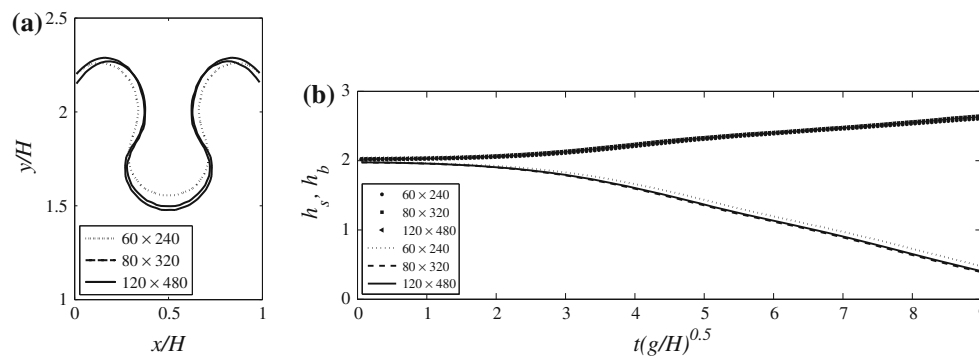

Fig. 14 Particle convergence for a test case with the Atwood number of $A_T = 1/3$ and the stability parameter of $\phi = 0.4$ on three different sets of particles (i.e., 60×240 (coarse), 80×320 (intermediate), and 120×480 (fine)); **a** the interface position at dimensionless time of $t^* = 4.5$, and **b** the y-coordinates of the tip of the falling (spike) and rising (bubble) fluid versus dimensionless time
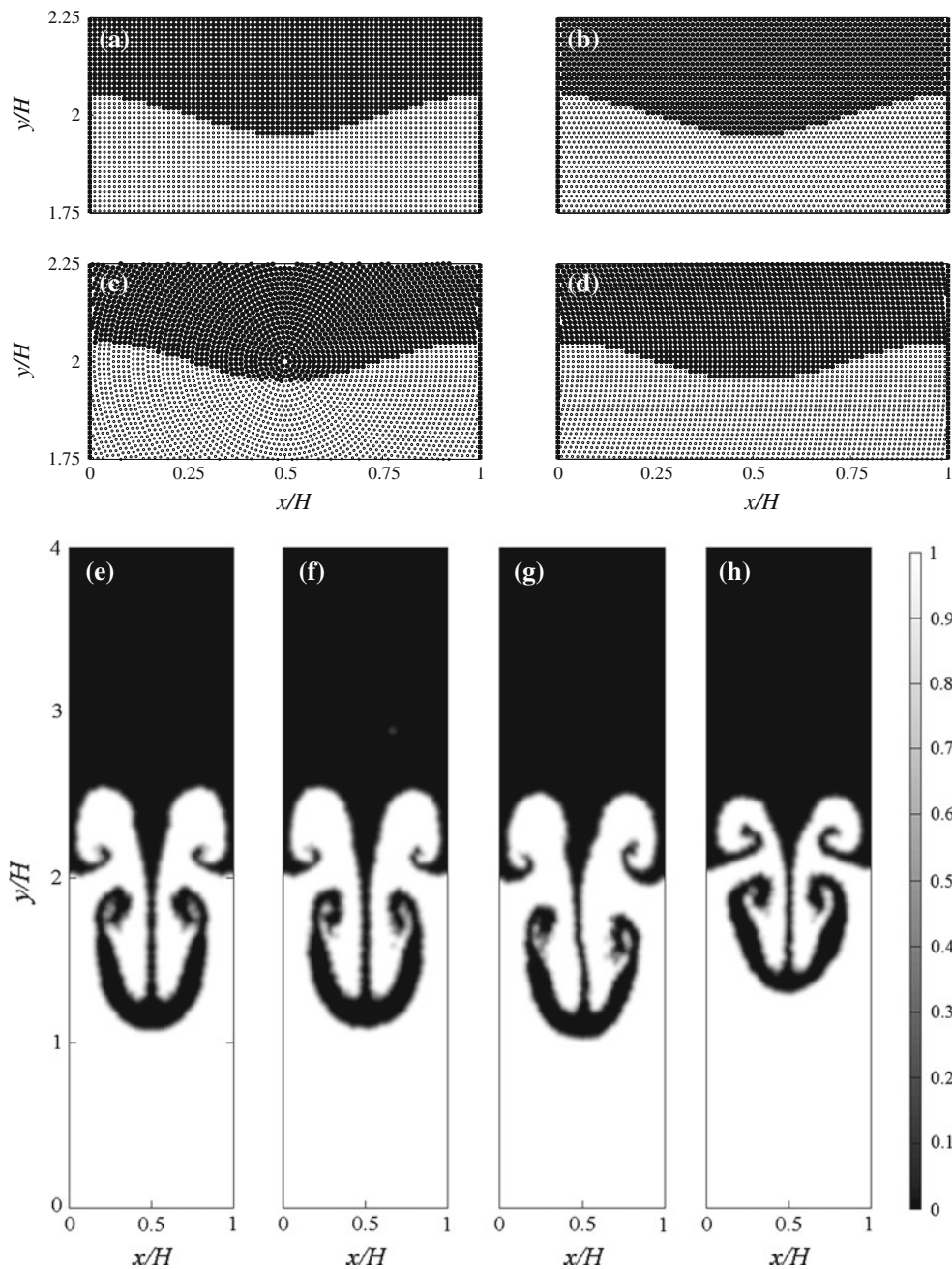
Fig. 15 The different initial particle distributions namely, **a** cubic, **b** staggered, **c** radially-centered, and **d** radially-off-centered, and in sub figures **e**, **f**, **g** and **h** are given the evolutions of the fluid interface of the single mode RTI for the Atwood number of $A_T = 1/3$ at dimensionless time of $t^* = t(g/H)^{0.5} = 5.4$ calculated correspondingly on the grids in sub figures **a**, **b**, **c** and **d**. It is noted that sub figure **h** has the lowest initial disturbance amplitude (0.044) and highest tip position with respect to the bottom wall of the domain which might explain the lag in the presented position of the tip of the spike

linear growth rate and terminal bubble velocity as well as Froude number agree well quantitatively with the theoretical predictions and previous numerical simulations. Furthermore, for the stability parameter analysis, some deviations from analytical results were noted, which were discussed and reasoned in details.

References

1. Rayleigh L (1883) Investigation of the character of the equilibrium of an incompressible heavy fluid of variable density. Proc Lond Math Soc 14(1):170–177
2. Taylor G (1950) The instability of liquid surfaces when accelerated in a direction perpendicular to their planes. I. Proc R Soc Lond A 201:192–196
3. Waddell JT, Niederhaus CE, Jacobs JW (2001) Experimental study of Rayleigh–Taylor instability: low Atwood number liquid systems with single-mode initial perturbations. Phys Fluids 13:1263
4. Andrews MJ, Dalziel SB (2010) Small Atwood number Rayleigh–Taylor experiments. Philos Trans R Soc A 368(1916):1663
5. Piriz AR, Cortazar OD, Cela JJL, Tahir NA (2006) The Rayleigh–Taylor instability. Am J Phys 74:1095
6. Mikaelian KO (1993) Effect of viscosity on Rayleigh–Taylor and Richtmyer–Meshkov instabilities. Phys Rev E 47(1):375
7. Youngs DL (1984) Numerical simulation of turbulent mixing by Rayleigh–Taylor instability. Phys D 12(1–3):32–44
8. Pullin D (1982) Numerical studies of surface-tension effects in nonlinear Kelvin–Helmholtz and Rayleigh–Taylor instability. J Fluid Mech 119(1):507–532
9. Bell JB, Marcus DL (1992) A second-order projection method for variable-density flows* 1. J Comput Phys 101(2):334–348
10. Brackbill JU, Kothe DB, Zemach C (1992) A continuum method for modeling surface tension* 1. J Comput Phys 100(2):335–354
11. Puckett EG, Almgren AA, Bell JB, Marcus DL, Rider WJ (1997) A high-order projection method for tracking fluid interfaces in variable density incompressible flows* 1. J Comput Phys 130(2):269–282
12. Scardovelli R, Zaleski S (1999) Direct numerical simulation of free-surface and interfacial flow. Annu Rev Fluid Mech 31(1):567–603
13. Tryggvason G (1988) Numerical simulations of the Rayleigh–Taylor instability. J Comput Phys 75(2):253–282
14. Tryggvason G, Bunner B, Ebrat O, Tauber W (1998) Computations of multiphase flows by a finite difference/front tracking method. I. Multi-fluid flows. Lecture series—Von Karman Institute for Fluid Dynamics, Sint-Genesius-Rode
15. Ding H, Spelt PDM, Shu C (2007) Diffuse interface model for incompressible two-phase flows with large density ratios. J Comput Phys 226(2):2078–2095
16. Oevermann M, Klein R, Berger M, Goodman J (2000) A projection method for two-phase incompressible flow with surface tension and sharp interface resolution. Konrad-Zuse-Zentrum für Informationstechnik, Berlin
17. Cummins SJ, Rudman M (1999) An SPH projection method. J Comput Phys 152(2):584–607
18. Tartakovsky AM, Meakin P (2005) A smoothed particle hydrodynamics model for miscible flow in three-dimensional fractures and the two-dimensional Rayleigh–Taylor instability. J Comput Phys 207(2):610–624
19. Hu XY, Adams NA (2007) An incompressible multi-phase SPH method. J Comput Phys 227(1):264–278
20. Shao S, Lo EYM (2003) Incompressible SPH method for simulating Newtonian and non-Newtonian flows with a free surface. Adv Water Resour 26(7): 787–800
21. Grenier N, Antuono M, Colagrossi A, Le Touzé D, Alessandrini B (2009) An Hamiltonian interface SPH formulation for multi-fluid and free surface flows. J Comput Phys 228(22):8380–8393
22. Shadloo MS, Zainali A, Yildiz M, Suleman A (2012) A robust weakly compressible SPH method and its comparison with an incompressible SPH. Int J Numer Methods Eng 89:939–956

23. Shadloo MS, Yildiz M (2011) Numerical modeling of Kelvin–Helmholtz instability using smoothed particle hydrodynamics. Int J Numer Methods Eng 87:988–1006
24. Hoover WG (1998) Isomorphism linking smooth particles and embedded atoms. Phys A 260(3):244–254
25. Gingold RA, Monaghan JJ (1977) Smoothed particle hydrodynamics-theory and application to non-spherical stars. Mon Notices R Astron Soc 181:375–389
26. Lucy LB (1977) A numerical approach to the testing of the fission hypothesis. Astron J 82:1013–1024
27. Fatehi R, Manzari M (2012) A consistent and fast weakly compressible smoothed particle hydrodynamics with a new wall boundary condition. Int J Numer Methods Fluids 68:905–921
28. Rafiee A, Thiagarajan KP (2009) An SPH projection method for simulating fluid-hypoelastic structure interaction. Comput Methods Appl Mech Eng 198(33–36):2785–2795
29. Hashemi MR, Fatehi R, Manzari MT (2011) SPH simulation of interacting solid bodies suspended in a shear flow of an Oldroyd-B fluid. J Non-Newton Fluid Mech 166:1239–1252
30. Monaghan JJ (2005) Smoothed particle hydrodynamics. Rep Prog Phys 68:1703
31. Randles PW, Libersky LD (1996) Smoothed particle hydrodynamics: some recent improvements and applications. Comput Methods Appl Mech Eng 139(1):375–408
32. Liu WK, Jun S, Zhang YF (1995) Reproducing kernel particle methods. Int J Numer Methods Fluids 20(8–9):1081–1106
33. Chen JS, Pan C, Wu CT, Liu WK (1996) Reproducing kernel particle methods for large deformation analysis of non-linear structures. Comput Methods Appl Mech Eng 139(1):195–227
34. Jun S, Liu WK, Belytschko T (1998) Explicit reproducing kernel particle methods for large deformation problems. Int J Numer Methods Eng 41(1):137–166
35. Liu WK, Jun S, Li S, Adee J, Belytschko T (1995) Reproducing kernel particle methods for structural dynamics. Int J Numer Methods Eng 38(10):1655–1679
36. Liu WK, Jun S, Sihling DT, Chen Y, Hao W (1997) Multiresolution reproducing kernel particle method for computational fluid dynamics. Int J Numer Methods Fluids 24(12):1391–1415
37. Chen JK, Beraun JE (2000) A generalized smoothed particle hydrodynamics method for nonlinear dynamic problems. Comput Methods Appl Mech Eng 190(1):225–239
38. Shadloo MS, Zainali A, Sadek S, Yildiz M (2011) Improved incompressible smoothed particle hydrodynamics method for simulating flow around bluff bodies. Comput Methods Appl Mech Eng 200:1008–1020
39. Morris JP (2000) Simulating surface tension with smoothed particle hydrodynamics. Int J Numer Methods Fluids 33(3):333–353
40. Yildiz M, Rook RA, Suleman A (2009) SPH with the multiple boundary tangent method. Int J Numer Methods Eng 77(10):1416–1438
41. Ginzburg I, Wittum G (2001) Two-phase flows on interface refined grids modeled with VOF, staggered finite volumes, and spline interpolants. J Comput Phys 166(2):302–335
42. Lafaurie B, Nardone C, Scardovelli R, Zaleski S, Zanetti G (1994) Modelling merging and fragmentation in multiphase flows with SURFER. J Comput Phys 113(1):134–147
43. Chandrasekhar S (1961) Hydrodynamic and hydromagnetic stability. Dover, New York
44. Guermond JL, Quartapelle L (2000) A projection FEM for variable density incompressible flows. J Comput Phys 165(1):167–188
45. Ramaprabhu P, Dimonte G, Andrews MJ (2005) A numerical study of the influence of initial perturbations on the turbulent Rayleigh–Taylor instability. J Fluid Mech 536(1):285–319

46. Goncharov VN (2002) Analytical model of nonlinear, single-mode, classical Rayleigh–Taylor instability at arbitrary Atwood numbers. Phys Rev Lett 88(13):134502

47. Abarzhi SI, Nishihara K, Glimm J (2003) Rayleigh–Taylor and Richtmyer–Meshkov instabilities for fluids with a finite density ratio. Phys Lett A 317(5–6):470–476

48. Scorer RS (1957) Experiments on convection of isolated masses of buoyant fluid. J Fluid Mech 2(6):583–594

49. Ramaprabhu P, Dimonte G, Young YN, Calder AC, Fryxell B (2006) Limits of the potential flow approach to the single-mode Rayleigh–Taylor problem. Phys Rev E 74(6):066308

50. Wilkinson JP, Jacobs JW (2007) Experimental study of the single-mode three-dimensional Rayleigh–Taylor instability. Phys Fluids 19:124102